Supporting Information
Bypassing nonlocal phenomena in metals using phonon-polaritons

Jacob T. Heiden,[1], Eduardo J. C. Dias,[2] Minhyuk Kim,[3] Martin Nørgaard,[2] Vladimir A. Zenin,[4] Sergey G. Menabde,[1] Hu Young Jeong,[3] N. Asger Mortensen,[2,5,*] and Min Seok Jang[1,*]

[1] School of Electrical Engineering, Korea Advanced Institute of Science and Technology (KAIST), Daejeon 34141, Korea

[2] POLIMA—Center for Polariton-driven Light–Matter Interactions, University of Southern Denmark, Campusvej 55, DK-5230 Odense M, Denmark

[3] Graduate School of Semiconductor Materials and Devices Engineering, Ulsan National Institute of Science and Technology (UNIST), Ulsan 44919, Korea

[4] Center for Nano Optics, University of Southern Denmark, Campusvej 55, DK-5230 Odense M, Denmark

[5] Danish Institute for Advanced Study, University of Southern Denmark, Campusvej 55, DK-5230 Odense M, Denmark

Contents

S1. Detailed theoretical description

A. General formalism

We consider a general heterostructure comprising N layers stacked along the z-direction, described by their permittivity ϵ_j ($j = 1, \cdots, N$) and thickness d_j ($j = 2, \cdots, N-1$). Between each layer j and $j+1$, we allow for the presence of a general surface conductivity σ_j ($j = 1, \cdots, N-1$). We note that, to describe anisotropic materials (such as hBN in this work), ϵ_j may be treated as a tensor with different components in the in-plane ($\epsilon_{j,\parallel}$) and out-of-plane ($\epsilon_{j,\perp}$) directions with respect to the interfaces of the heterostructure.

In each layer j, the solution of Maxwell's equations for frequency ω and in-plane momentum q in the case of p-polarisation results in magnetic $\mathbf{H}_j(x,z) = H_j^y(x,z)\hat{y}$ and transverse electric fields $\mathbf{E}_j^{\mathrm{T}}(x,z) = E_j^{\mathrm{T},x}(x,z)\hat{x} + E_j^{\mathrm{T},z}(x,z)\hat{z}$ defined by:

$$H_j^y(x,z) = \left(a_j^- \mathrm{e}^{-\mathrm{i}k_{j,z}z} + a_j^+ \mathrm{e}^{\mathrm{i}k_{j,z}z}\right)\mathrm{e}^{\mathrm{i}qx}, \tag{S1a}$$

$$E_j^{\mathrm{T},x}(x,z) = \left(\frac{k_{j,z}}{\epsilon_j k}\right)\left(-a_j^- \mathrm{e}^{-\mathrm{i}k_{j,z}z} + a_j^+ \mathrm{e}^{\mathrm{i}k_{j,z}z}\right)\mathrm{e}^{\mathrm{i}qx}, \tag{S1b}$$

$$E_j^{\mathrm{T},z}(x,z) = \left(\frac{-q}{\epsilon_j k}\right)\left(a_j^- \mathrm{e}^{-\mathrm{i}k_{j,z}z} + a_j^+ \mathrm{e}^{\mathrm{i}k_{j,z}z}\right)\mathrm{e}^{\mathrm{i}qx}, \tag{S1c}$$

where $k = \omega/c$ and $k_{j,z} = \sqrt{\epsilon_j k^2 - q^2}$ (with the square root taken to yield a positive imaginary part). For a layer j composed of an anisotropic material, ϵ_j in Eqs. (S1b) and (S1c) needs to be replaced respectively by $\epsilon_{j,\parallel}$ and $\epsilon_{j,\perp}$, and the corresponding out-of-plane wavevector becomes $k_{j,z} = \sqrt{\epsilon_{j,\parallel} k^2 - (\epsilon_{j,\parallel}/\epsilon_{j,\perp}) q^2}$ [1].

In dielectric layers that are accurately described locally, we take the full electric field to be transverse, that is, $\mathbf{E}_j(x,z) = \mathbf{E}_j^{\mathrm{T}}(x,z)$, with the components given by Eqs. (S1). Conversely, in metallic layers where nonlocal effects may be sizeable, we follow the hydrodynamical model (see details in Refs. [1, 2]) and supplement the total electric field with curl-free longitudinal components $\mathbf{E}_j^{\mathrm{L}}(x,z) = E_j^{\mathrm{L},x}(x,z)\hat{\mathrm{x}} + E_j^{\mathrm{L},z}(x,z)\hat{\mathrm{z}}$ given by:

$$E_j^{\mathrm{L},x}(x,z) = \left(\frac{q}{k}\right)\left(-b_j^- \mathrm{e}^{-\mathrm{i}k_{j,\mathrm{L}}z} + b_j^+ \mathrm{e}^{\mathrm{i}k_{j,\mathrm{L}}z}\right)\mathrm{e}^{\mathrm{i}qx}, \tag{S2a}$$

$$E_j^{\mathrm{L},z}(x,z) = \left(\frac{k_{j,\mathrm{L}}}{k}\right)\left(b_j^- \mathrm{e}^{-\mathrm{i}k_{j,\mathrm{L}}z} + b_j^+ \mathrm{e}^{\mathrm{i}k_{j,z}z}\right)\mathrm{e}^{\mathrm{i}qx}, \tag{S2b}$$

where, for a metal with a permittivity ϵ_j described by the Drude model (see Eq. (2) in the main text), we define the longitudinal wavevector $k_{j,\mathrm{L}} = \beta^{-1}\sqrt{\omega(\omega + \mathrm{i}\gamma_\mathrm{m}) - \omega_\mathrm{p}^2/\epsilon_\mathrm{b} - \beta^2 q^2}$ (with the square root taken to yield a positive imaginary part) that depends on the nonlocal parameter $\beta = \sqrt{3/5}v_F$ proportional to the Fermi velocity v_F of the electrons in the metal. The full electric field in such regions is thus described by $\mathbf{E}_j(x,z) = \mathbf{E}_j^{\mathrm{T}}(x,z) + \mathbf{E}_j^{\mathrm{L}}(x,z)$.

The problem of finding the modes supported by such heterostructure becomes finally the problem of determining the coefficients $a^\pm$ and $b^\pm$ in each layer, which depend on the external illumination conditions of the problem.

1. *With external illumination.* The usual Fresnel coefficients can be obtained by assuming top-side light plane wave incidence on the structure, for which we take $a_1^- = 1$ and $a_N^+ = 0$. From here we can also identify $a_1^+ = r_\mathrm{p}$ and $a_N^- = t_\mathrm{p}$ (the latter is the transmittance coefficient of the combined structure when the $(N-1)$th layer is not metallic). Additionally, if the $(N-1)$th layer is metallic, we set $b_N^+ = 0$ and define $b_N^- = \tau_\mathrm{p}$, where the latter can be understood as a *nonlocal* transmittance coefficient (however, note that the actual transmittance into the metal now depends on both t_p and τ_p). We remark that we are defining the reflectance and transmittance coefficients of the system with respect to the amplitude of the associated magnetic fields (and not electric fields). We remain with $2(N-1) + N_\mathrm{m}$ unknown coefficients in the problem, where N_m is the number of nonlocal metal/dielectric interfaces in the heterostructure (for simplicity, we do not consider here the case of two consecutive nonlocal metallic layers). These coefficients can be determined by the boundary conditions at each interface, primarily the continuity of the tangential component of the electric field, and the discontinuity of the tangential component of the magnetic field when in the presence of a current density in the interface. These amount to $2(N-1)$ conditions that can be written for the interface between layers j and $j+1$ (located at $z_1 = 0$ for $j = 1$ and $z_j = z_{j-1} - d_j$ for $j > 1$) as

$$E_j^x(x,z_j) - E_{j-1}^x(x,z_j) = 0, \tag{S3a}$$

$$H_j^y(x,z_j) - H_{j-1}^y(x,z_j) = 4\pi(\sigma_j/c)E_j^x(x,z_j). \tag{S3b}$$

The remaining N_m boundary conditions correspond to the vanishing of the normal component of the free-charge polarisation vector $\mathbf{P} = (\mathrm{i}/k)\nabla \times \mathbf{H} - \epsilon_\mathrm{b}\mathbf{E}$ at each of the metal/dielectric interfaces, which can be rewritten as

$$P_j^z(x,z_j) = -(q/k)H_j^y(x,z_j) - \epsilon_\mathrm{b}E_j^z(x,z_j) = 0. \tag{S3c}$$

Equations (S3) together with Eqs. (S1) and (S2) form a system of $2(N-1) + N_\mathrm{m}$ equations and $2(N-1) + N_\mathrm{m}$ unknowns that can straightforwardly be solved to yield all unknown coefficients of the system.

The frequency- and wavevector-dependent reflectance coefficient $r_\mathrm{p}(\omega, q)$ of the combined structure, from where the supported modes follow from solving the equation $1/r_\mathrm{p} = 0$.

2. *Without external illumination.* Alternatively, the pure polaritonic fields (i.e. in the absence of external illumination) can be obtained by setting $a_1^- = 0$ and normalizing all other coefficients of the system to a_1^+, which becomes a normalisation parameter of the problem. Employing the same boundary conditions as above, we obtain $2(N-1) + N_\mathrm{m}$ equations and $2(N-1) + N_\mathrm{m} - 1$ coefficients –the extra equation can be used to determine the dispersion relation of the modes (which should coincide with the solution of $1/r_\mathrm{p} = 0$).

   The spatial- and frequency-dependent energy density associated with the polaritonic fields follows as

$$U(x,z) = \frac{1}{8\pi}\left[|\mathbf{H}(x,z)|^2 + \tilde{\epsilon}|\mathbf{E}(x,z)|^2\right], \tag{S4}$$

   where we introduce $\tilde{\epsilon} = \mathrm{Re}\{d(\omega\epsilon)/d\omega\}$. In anisotropic materials (e.g. hBN), the second term in the square brackets must be rewritten as $\tilde{\epsilon}_\parallel |E_x(x,z)|^2 + \tilde{\epsilon}_\perp |E_z(x,z)|^2$, with $\tilde{\epsilon}_s = \mathrm{Re}\{d(\omega\epsilon_s)/d\omega\}$ ($s = \parallel, \perp$). The total energy associated with the polaritonic field (per unit length along the transverse direction) can then be written as $U_\mathrm{T} = 2\int_0^\infty dx \int_{-\infty}^\infty dz\, U(x,z)$. In the energy density plots of Fig. 2 in the main text, we choose the normalisation constant a_1^+ such that U_T is independent of the spacing thickness d and proportional to $\hbar\omega$ (that is, the field corresponds to that of a single polariton per unit of transverse length).

B. Closed-form expressions for single and double interfaces

The formalism above can be applied to find analytically all coefficients that fully determine the electric and magnetic fields in a general heterostructure of arbitrary number N of layers. However, the general closed-form expression of such coefficients can be very cumbersome, except in the special cases of heterostructures with just a few layers. In Table S1, we summarise the analytical solutions for such coefficients in the cases of heterostructures with 1 or 2 interfaces, where the last layer is a nonlocal metal, both for the cases where there is or is not external illumination as a source (see schemes present in the first column of Table S1). In the case of the double interface, the results admit the incorporation of a surface conductivity σ between the two dielectric regions. Furthermore, we define for convenience reasons the nonlocal parameter

$$\Omega = (q^2/k_\mathrm{L})(\epsilon_\mathrm{b} - \epsilon_3)\epsilon_1/\epsilon_\mathrm{b}, \tag{S5}$$

and introduce the usual Fresnel coefficients between local media of permittivity ϵ_i and ϵ_j as

$$r^{ij}_{\mathrm{p},0} = \frac{\epsilon_\mathrm{j} k_{z,i} - \epsilon_i k_{z,j} + 4\pi(\sigma_{ij}/c)k_{z,i}k_{z,j}/k}{\epsilon_\mathrm{j} k_{z,i} + \epsilon_i k_{z,j} + 4\pi(\sigma_{ij}/c)k_{z,i}k_{z,j}/k}, \tag{S6a}$$

$$t^{ij}_{\mathrm{p},0} = \frac{2\epsilon_\mathrm{j} k_{z,i}}{\epsilon_\mathrm{j} k_{z,i} + \epsilon_i k_{z,j} + 4\pi(\sigma_{ij}/c)k_{z,i}k_{z,j}/k}, \tag{S6b}$$

where σ_{ij} is the surface conductivity in the interface between the two regions. We note that the case of anisotropic materials (such as hBN) can be readily recovered with the modifications stated above. In all cases, the dispersion relation of the modes supported by each structure can be obtained by solving the equation $\Delta = 0$. For the case without source, the factor A is arbitrary and can be chosen as a normalisation factor of the problem.

C. Graphene nonlocal conductivity

In the graphene/gap/Au heterostructures, we model graphene as a nonlocal interfacial surface conductivity modelled at zero temperature as $\sigma_\mathrm{G}(\omega, q) = -\mathrm{i}\omega\chi(\omega, q)$, where we introduce the bare

Table S1. Generalised Fresnel coefficients for heterostructures composed by single and double interfaces and nonlocal metals. The first column shows the two types of heterostructures considered and defines all relevant coefficients in the corresponding schemes. Additional functions Ω, $r^{ij}_{p,0}$, and $t^{ij}_{p,0}$ are defined in Eqs. (S5) and (S6). The dispersion relation of the modes supported by the structure can be obtained by solving $\Delta = 0$. The coefficient A is a normalisation factor of the problem.

	Coefficient	Single interface	Double interface
With source	Δ	$\epsilon_3 k_{z1} + \epsilon_1 k_{z3} + \Omega$	$1 - r^{21}_{\mathrm{p},0} r^{23}_{\mathrm{p}} \mathrm{e}^{2\mathrm{i}k_{z,2}d}$
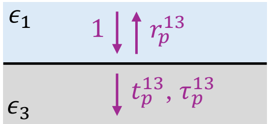	$a_1^+ = r_p$	$\frac{\epsilon_3 k_{z1} - \epsilon_1 k_{z3} - \Omega}{\Delta} \equiv r^{13}_p$	$r^{12}_{\mathrm{p},0} + \frac{t^{12}_{\mathrm{p},0} r^{23}_{\mathrm{p}} t^{21}_{\mathrm{p},0} \mathrm{e}^{2\mathrm{i}k_{z,2}d}}{\Delta}$
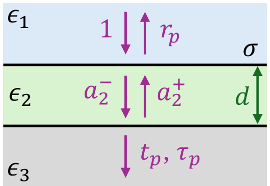	a_2^-	-	$\frac{t^{12}_{\mathrm{p},0}}{\Delta} \mathrm{e}^{-\mathrm{i}k_{z,3}d}$
	a_2^-	-	$\frac{t^{12}_{\mathrm{p},0} r^{23}_{\mathrm{p}} \mathrm{e}^{2\mathrm{i}k_{z,2}d}}{\Delta} \mathrm{e}^{-\mathrm{i}k_{z,3}d}$
	$a_3^- = t_p$	$\frac{2\epsilon_3 k_{z1}}{\Delta} \equiv t^{13}_p$	$\frac{t^{12}_{\mathrm{p},0} t^{23}_{\mathrm{p}} \mathrm{e}^{\mathrm{i}k_{z,2}d}}{\Delta} \mathrm{e}^{-\mathrm{i}k_{z,3}d}$
	$b_3^- = \tau_p$	$\left(\frac{\Omega}{q\epsilon_1\epsilon_3}\right) t^{13}_{\mathrm{p}} \equiv \tau^{13}_p$	$\frac{t^{12}_{\mathrm{p},0} \tau^{23}_{\mathrm{p}} \mathrm{e}^{\mathrm{i}k_{z,2}d}}{\Delta} \mathrm{e}^{-\mathrm{i}k_{\mathrm{L},3}d}$
Without source	a_1^+	A	A
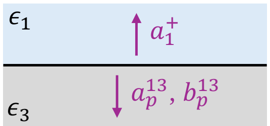	a_2^-	-	$\frac{a^{12}_p}{1 + r^{23}_p \mathrm{e}^{2\mathrm{i}k_{z2}d}}$
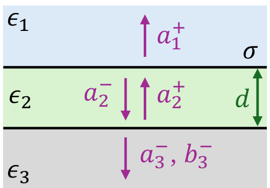	a_2^+	-	$\frac{a^{12}_p r^{23}_p \mathrm{e}^{2\mathrm{i}k_{z2}d}}{1 + r^{23}_p \mathrm{e}^{2\mathrm{i}k_{z2}d}}$
	a_3^-	$-A\frac{\epsilon_3 k_{z1}}{\epsilon_1 k_{z3} + \Omega} \equiv a^{13}_p$	$\frac{a^{12}_p t^{23}_p \mathrm{e}^{2\mathrm{i}k_{z2}d}}{1 + r^{23}_p \mathrm{e}^{\mathrm{i}k_{z2}d}} \mathrm{e}^{-\mathrm{i}k_{z3}d}$
	b_3^-	$\left(\frac{\Omega}{q\epsilon_1\epsilon_3}\right) a_3^- \equiv b^{13}_p$	$\frac{a^{12}_p \tau^{23}_p \mathrm{e}^{\mathrm{i}k_{z2}d}}{1 + r^{23}_p \mathrm{e}^{\mathrm{i}k_{z2}d}} \mathrm{e}^{-\mathrm{i}k_{\mathrm{L},3}d}$

susceptibility (in absence of losses)

$$\chi_0(\omega, q) = \frac{2e^2\omega}{\pi\hbar v_{\mathrm{F,G}}} \left[\frac{k_{\mathrm{F}}}{q^2} + \frac{[G(\Delta_-) - G(-\Delta_-) + \mathrm{i}\pi]\Theta(\mathrm{Re}\{\Delta_-\} + 1) + G(-\Delta_-) - G(\Delta_+)}{8\sqrt{\omega^2/v_{\mathrm{F,G}}^2 - q^2}} \right], \tag{S7}$$

where $v_{\mathrm{F,G}} \approx c/300$ is the Fermi velocity of electrons in graphene, $k_{\mathrm{F}} = E_{\mathrm{F}}/\hbar v_{\mathrm{F,G}}$, $\Delta_\pm = (\omega/v_{\mathrm{F,G}} \pm 2k_{\mathrm{F}})/q$, $G(z) = z\sqrt{z^2-1} - \log(z + \sqrt{z^2-1})$ (with the square root taken to yield positive imaginary parts and the imaginary part of the log function taken in the $[-\pi, \pi)$ sheet); and we add a phenomenological damping rate γ using the Mermin prescription [3]:

$$\chi(\omega, q) = \frac{(1 + \mathrm{i}\gamma/\omega)\chi_0(\omega + \mathrm{i}\gamma, q)}{1 + (\mathrm{i}\gamma/\omega)\chi_0(\omega + \mathrm{i}\gamma, q)/\chi_0(0, q)}. \tag{S8}$$

S2. Nonlocal metal response of polaritons

As the main text explores, the nonlocal response of Au differs drastically between hyperbolic image phonon-polaritons (HIPs) and acoustic graphene plasmons (AGPs). Since both systems are fundamentally governed by mode screening from the metallic substrate, their comparison – as shown in figure 1 and 2 of the main paper – is instructive for understanding nonlocal effects. Here, we compare various aspects of both modes to develop a more complete picture of why the HIP eigenmode remains predominantly local.

A. Field distributions and the role of nonlocal effects

We start by studying the nonlocal influence on the spatial field distributions for a 10 nm hBN slab on Au at a frequency of $1500\,\mathrm{cm}^{-1}$ (Fig. S1a-c). Evidently, the inclusion of nonlocal effects in Au's response does not alter the field intensities in hBN much even though the phase velocity of the mode is approaching $v_{F,\mathrm{Au}}$. However, the more interesting point of focus is in Au: in the local case, as expected of good metals, both the $E_x(z)$ and $E_z(z)$ field are several orders of magnitude weaker than in hBN. Introducing nonlocality, however, tells another story – revealing a small field penetration into the Au, particularly for the $E_z(z)$ field (inset of Fig. S1b), extending ≈ 1 nm before decaying to similar values as in the local case. Since the magnetic field is entirely transverse in nature and nonlocality enters through longitudinal components, the nonlocal $H(z)$ field only deviates slightly from its local counterpart, a difference caused by a slight change in q.
Decreasing the hBN thickness to 1 nm results in more significant changes in the spatial field distributions (Fig. S1d-f). The field penetration into Au has increased, especially $E_x(z)$ (inset of Fig. S1d) is orders of magnitude higher than for for the 10 nm case. Another notable observation is the general decrease of the field amplitude in hBN and air; however, we again contribute this to the change in q. Turning to our point of reference, the AGP eigenmode, we observe that the field is likewise highly confined in the gap; however, even at a gap thickness of 10 nm the fields are heavily influenced by the inclusion of nonlocal effects (Fig. S1g-i) – to a similar extent as the HIP mode with a 1 nm thick hBN slab – and a large $E_z(z)$ field penetration into Au is apparent (Fig. S1h). This field penetration only becomes larger as the mode is vertically compressed further (Fig. S1j-l); while the fields remains at a larger amplitude in the gap than the Au, the energy density is almost entirely located in the metal due to the large discrepancy in permittivity between the two media (Fig. 2 of the main paper).

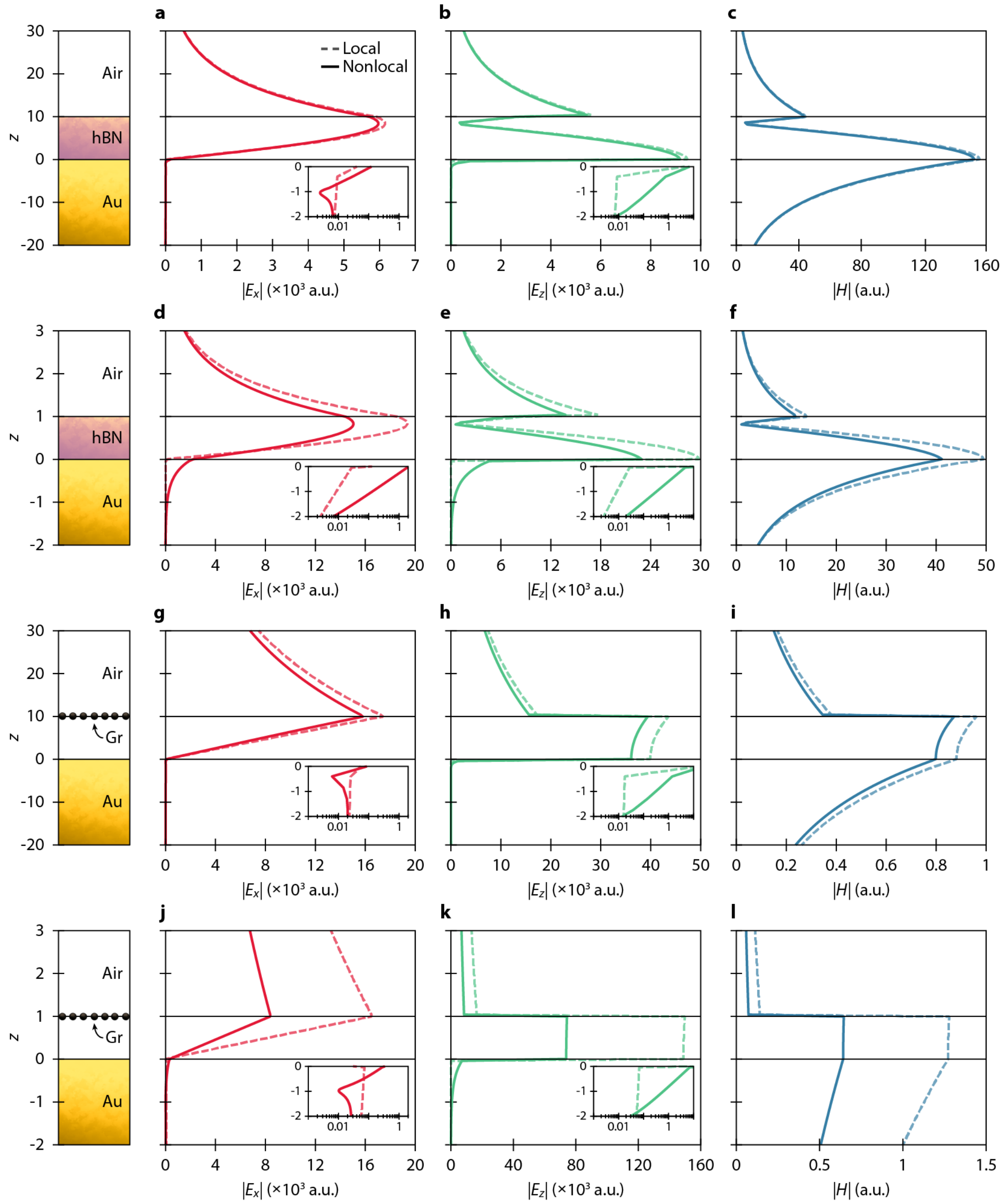

Figure S1. Spatial field distribution of HIP and AGP eigenmodes. Results are calculated using both local (dashed) and nonlocal (solid) metal formalisms at a frequency of 1500 cm^{-1}. The HIP-supporting heterostructure consists of an air/hBN/Au stack (schematic on the left). **a**, $|E_x|$ profile of the HIP eigenmode for an hBN thickness of 10 nm. **b**,**c**, same as (**a**) but for $|E_z|$ and $|H|$, respectively. **d**-**f**, same as (**a**-**c**) but for 1 nm hBN. **g**-**l**, same as (**a**-**f**) but for the AGP eigenmode. The AGP-supporting heterostructure consists of an air/graphene/air gap/Au stack (schematic on the left). Graphene conductivity is always described through its nonlocal response. Insets in the $|E_x|$ and $|E_z|$ fields highlight the field penetration into Au. All fields are normalised as described in Section S1.

B. Perturbation strength comparison

As discussed in the main text, HIPs provide approximately an order of magnitude greater lateral confinement compared to AGPs for the same degree of vertical confinement (Fig. S2a). Both systems exhibit a similar ratio of $\mathrm{Re}(q)_{\mathrm{loc}}/\mathrm{Re}(q)_{\mathrm{non-loc}}$ as a function of hBN or spacer thickness until the HIP ratio begins to saturate at an hBN thickness of around 1 nm (Fig. S2b). At this thickness, both modes reveal a frequency-dependent q discrepancy between local and nonlocal predictions of around $\approx 8\%$ at a frequency of $1500\,\mathrm{cm}^{-1}$. However, while the AGP mode exhibits $\mathrm{Re}(q)_{\mathrm{AGP}} \simeq 11 \times 10^5\,\mathrm{cm}^{-1}$ with $n_{\mathrm{eff,AGP}} \simeq 115$, the HIP mode achieves significantly greater confinement, with $\mathrm{Re}(q)_{\mathrm{HIP}} \simeq 120 \times 10^5\,\mathrm{cm}^{-1}$ and $n_{\mathrm{eff,AGP}} \simeq 1250$. Importantly, the q discrepancy for the AGP mode continues to grow due to the fundamental restriction imposed by $v_{F,\mathrm{G}}$ and the additional contribution to nonlocality from $v_{F,\mathrm{Au}}$, which ultimately prevents the mode from bypassing these critical velocities (Fig. S2c).

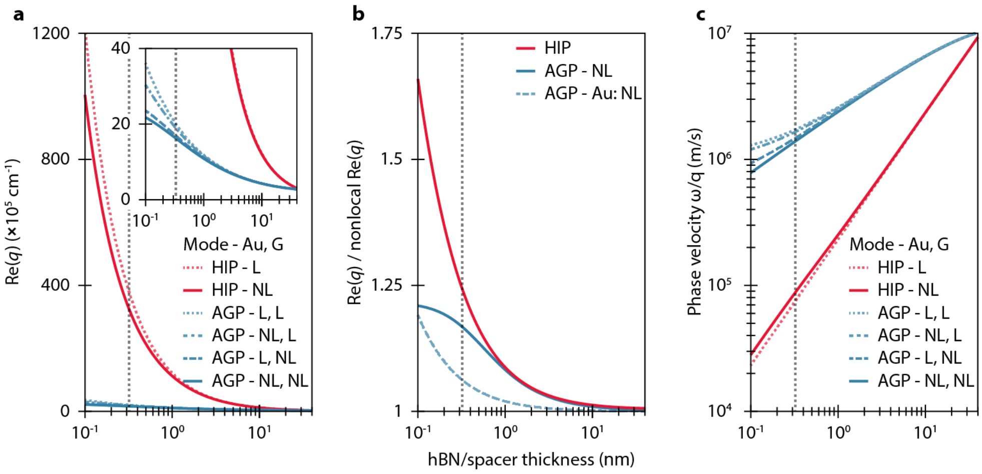

Figure S2. Nonlocal perturbation comparison of HIP and AGP mode. a, Theoretical predictions of Re(q) as a function of hBN or spacer thickness for a variety of cases at a frequency of $1500\,\mathrm{cm}^{-1}$: HIP - L (local metal), HIP - NL (nonlocal metal), AGP - X, Y (X = {L, NL} for local/nonlocal metal, Y = {L, NL} for local/nonlocal graphene). The inset highlights the much lower lateral confinement of the AGP mode. **b**, Ratio of Re(q) for the local to nonlocal cases for the HIP mode, the AGP mode with both metal and graphene considered nonlocal, and the AGP mode with nonlocal metal and local graphene. **c**, Phase velocity predictions corresponding to the cases shown in (**a**).

Interestingly, the HIP mode exhibit a negative dispersive behaviour in relation to its nonlocal effects (Fig. S3a), while the nonlocal perturbation of AGP modes is more or less dispersionless (Fig. S3b,c). This effectively means that the nonlocal effects experienced by the HIP mode is not related only to q alone, but also the dispersive behaviour of $\epsilon_{\perp}$.

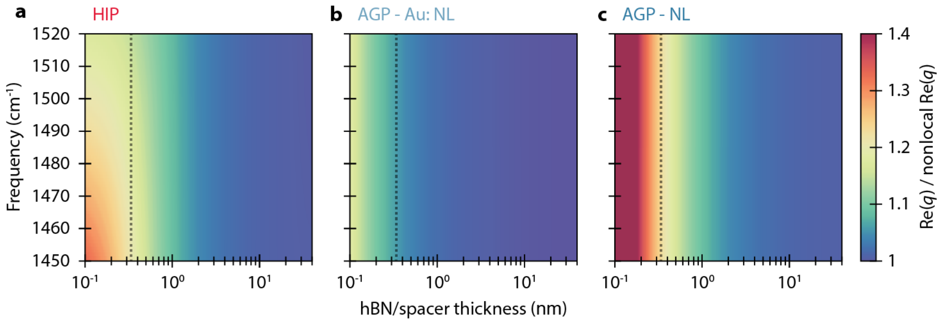

Figure S3. Frequency-dependant nonlocal perturbation comparison of HIP and AGP mode. a-c, Ratio of Re(q) for the local to nonlocal cases for the HIP mode, the AGP mode with nonlocal metal and local graphene, and the AGP mode with both metal and graphene considered nonlocal, respectively.

C. Energy density

Since we observe that the nonlocal perturbation – however small it may be – is theoretically expected to be negatively dispersive (Fig. S3a) we turn to the same analysis of integrated energy density as in the main paper. Figure S4a-f displays the results of this integration for both local (Fig. S4a-c) and nonlocal (Fig. S4d-f) metal formalisms in air (Fig. S4a,d), hBN (Fig. S4b,e) and Au (Fig. S4c,f). As the main paper highlights, Au is an excellent metal and therefore screens the phonon polaritons well, resulting in the energy density being highly concentrated in hBN. However, at $d \lesssim 10\,\mathrm{nm}$ – when approaching $v_{F,\mathrm{Au}}$ – this screening starts to slowly deteriorate; however, as mentioned in the main paper it does not become significant until much lower thicknesses. Regarding the dispersive behaviour we observe the same for energy density, albeit small: for 1 nm thick hBN, the energy density in the gold varies from 35.7% to 33.6% over the frequency range. Similar to the perturbation results, the integrated density of the AGP mode displays no dispersive behaviour (Fig. S4g-l).

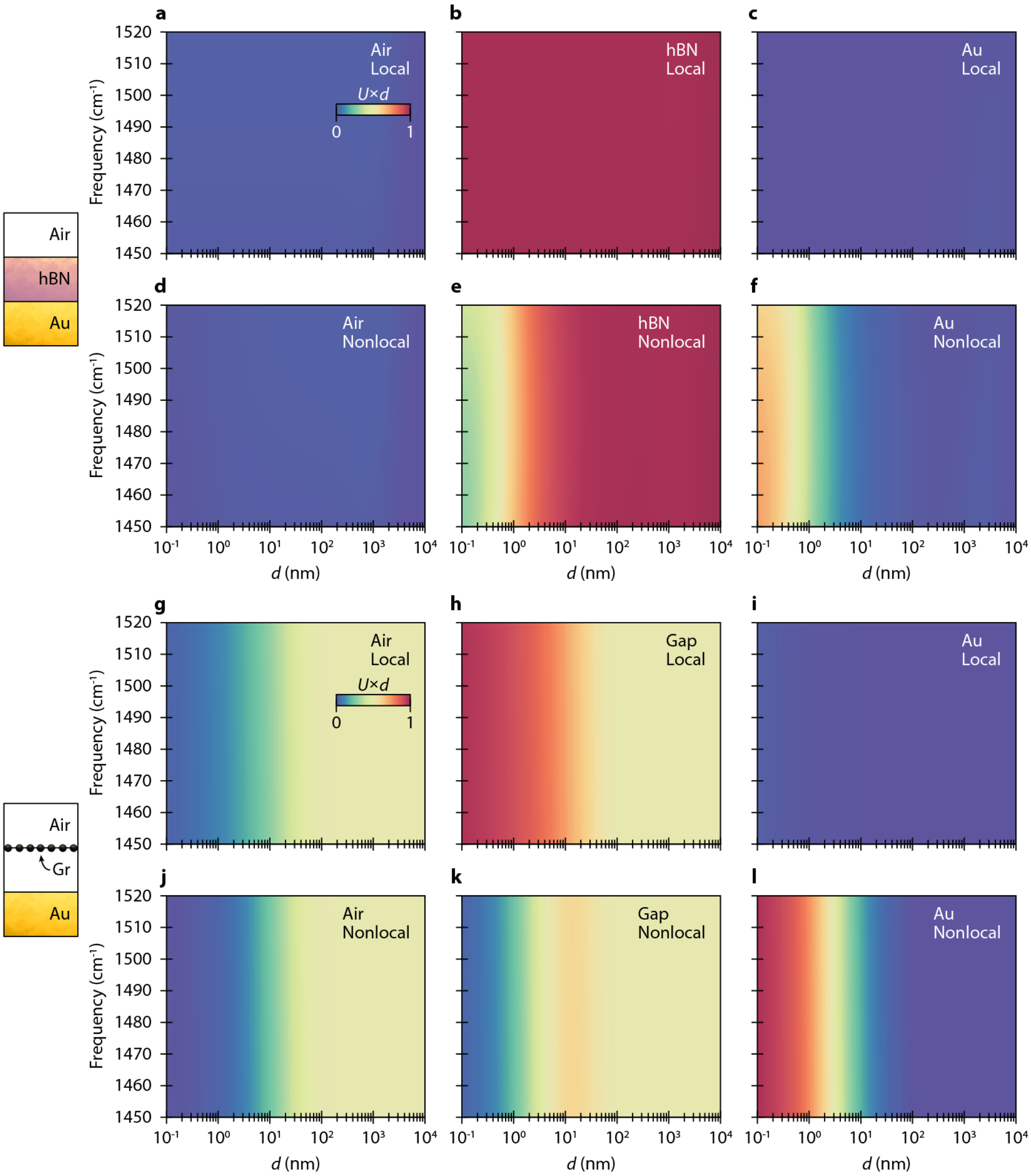

Figure S4. Integrated energy density as a function of distance and frequency. a-c, Integrated energy density, in the the HIP-supporting heterostructure (schematic on the left), shown as a percentage of the total energy density in the structure for the air (**a**), hBN (**b**), and Au (**c**) regions, calculated using the local metal formalism. **d-f**, same as (**a-c**) but calculated using the nonlocal metal formalism. **g-l**, same as (**a-f**) but for the AGP-supporting heterostructure (schematic on the left).

S3. Metal-dependent nonlocality: Au vs. Ti

It is well established that the nonlocal effects of a system depends heavily on the metal due to the different v_F and permittivity of varying metals [1, 4, 5]. Here we compare Au to Ti, since Ti is widely used as an adhesion layer in nanophotonics.

A. Field distributions of the Ti supported HIP mode

We start our investigation of nonlocal effects in HIP modes screened by Ti by analysing the spatial field distributions, following a similar approach to figure S1, at a frequency of 1500 cm^{-1}. With a Fermi velocity of $v_{F,\mathrm{Ti}} \simeq 1.79 \times 10^6$ m/s, Ti exhibits a seemingly minor velocity difference compared to Au $v_{F,\mathrm{Au}} \simeq 1.4 \times 10^6$ m/s. However, the impact of this difference is pronounced: when nonlocal effects are incorporated, significant field penetration into Ti is already evident for a 10 nm thick hBN layer (Fig. S5a-c). For 1 nm thick hBN this field penetration is further exacerbated (Fig. S5d-f), combined with the field amplitude in hBN being about halved, the $E_z(z)$ field does not experience the common discontinuity (Fig. S5e). These results indicate that HIP modes can experience significant nonclassical effects when screened by metals with weaker screening properties. Next, we examine the theoretical nonlocal perturbation caused by the field deviations in the hBN/Ti heterostructure.

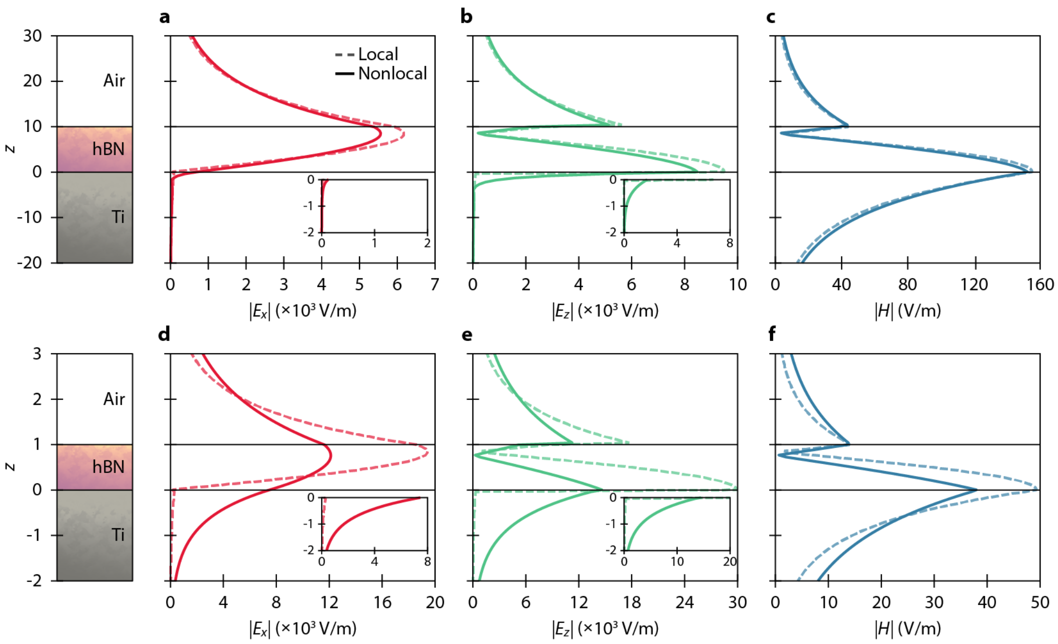

Figure S5. Spatial field distribution of HIP and AGP eigenmodes screened by Ti. Results are calculated using both local (dashed) and nonlocal (solid) metal formalisms at a frequency of 1500 cm^{-1}. The HIP-supporting heterostructure consists of an air/hBN/Ti stack (schematic on the left). **a**, $|E_x|$ profile of the HIP eigenmode for an hBN thickness of 10 nm. **b**,**c**, same as (**a**) but for $|E_z|$ and $|H|$, respectively. **d**-**f**, same as (**a**-**c**) but for 1 nm hBN. Insets in the $|E_x|$ and $|E_z|$ fields highlight the field penetration into Ti. All fields are normalised as described in Section S1.

B. Perturbation strength comparison

Based on the spatial field distribution, it is clear that HIPs screened by Ti should be significantly more nonlocal than those screened by Au. Here, we quantify and compare the perturbation strength like in figure S2 (Fig. S6). The pronounced discrepancies between the local and nonlocal fields in figure S5 correlate to a significant nonlocal perturbation of about 9% for a 10 nm thick hBN layer at a frequency of 1500 cm^{-1} – exceeding the perturbation felt by the HIP mode on Au with just a 1 nm hBN thickness. Notably, for 1 nm hBN on Ti, the discrepancy increases to nearly 60%, far surpassing the effect observed for the same thickness on Au. However, in the local limit, no discernible difference exists between Au and Ti (Fig. S6a), as both behave essentially as perfect metals in the mid-infrared frequency range. These theoretical predictions underscore the importance of carefully selecting materials in electromagnetic designs.

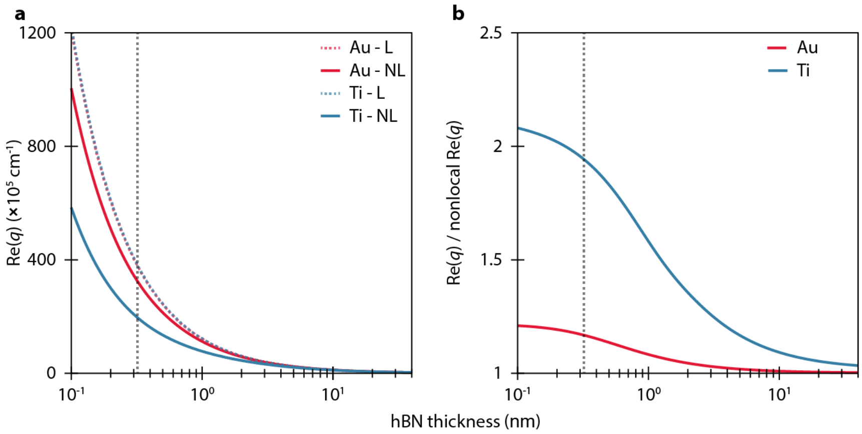

Figure S6. Nonlocal perturbation comparison of Au and Ti substrate impact on HIP mode. a, Local and nonlocal theoretical predictions of Re(q) as a function of hBN thickness for the cases of an Au and Ti substrate. **b**, Ratio of Re(q) for the local to nonlocal cases for the HIP modes.

C. Energy density

Similar to the case of Au, using Ti as a screening metal within a local formalism yields an energy density distribution almost entirely confined to the hBN, with minimal variation as a function of d (Fig. S7a). Adding nonlocal effects to the consideration, the distribution again follows a trend similar to the HIP mode screened by Au (Fig. 2b of the main paper); albeit with an earlier onset of metal penetration, becoming visually significant at $d \lesssim 5\,\text{nm}$ (Fig. S7b). Integrating U along the z-axis (Fig. S7c) confirms that the HIP mode stays well confined in the hBN; however, the earlier energy penetration results in a Ti contribution of approximately 10% at $d \simeq 15\,\text{nm}$, correlating well with the field profiles (Fig. S5). At $d \lesssim 0.7\,\text{nm}$ the Ti contribution becomes dominant.

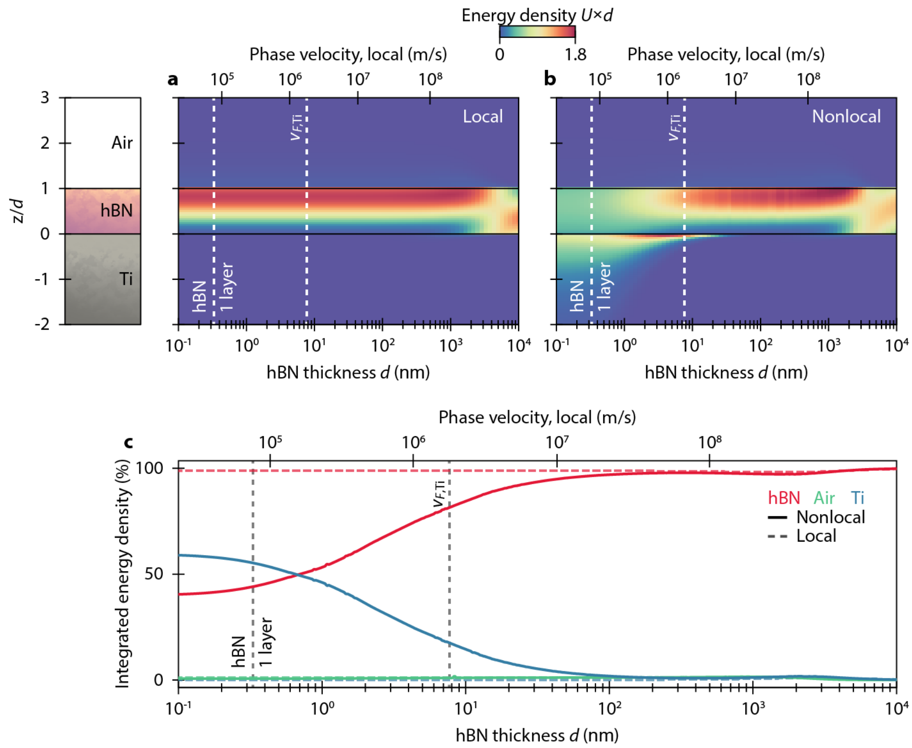

Figure S7. Energy density distribution. a,**b**, Local (**a**) and nonlocal (**b**) energy density U (multiplied by the spacing distance d) as a function of d and position along the HIP-supporting heterostructure (schematic on the left), at a frequency of $1500\,\text{cm}^{-1}$. **c**, Integrated energy density within the hBN (red), air (green), and Ti (blue) regions, as percentage of the total integrated energy density in the full structure, plotted as a function of d. Results are calculated within both local (dashed) and nonlocal (solid) metal formalisms.

S4. Near-field probing efficiency

In our s-SNOM experiments on HIPs, the vertical electric field component, E_z, extends above the structure, enabling effective coupling to the AFM tip. As the hBN layer becomes thinner, however, HIP confinement increases, reducing the E_z filed that extends above the heterostructure – ultimately setting a limit for the minimum hBN thickness at which HIPs can be effectively probed. To investigate this threshold, we solve Maxwell's equations in a multilayer configuration to identify the HIP mode uniquely supported by the structure (Local fields, Fig. S8a). Complementing this analytical solution, we perform full-wave finite-element-method (FEM) simulations (Comsol Multiphysics 5.4, Fig. S8a). We define the E_z penetration depth above hBN, D_e, as the point at which the field amplitude decays to $E_{z=d}\mathrm{e}^{-1}$.

The in-plane momentum of the HIP, and hence D_e, varies with both the hBN thickness d the excitation frequency ω, indicating that the effectiveness of the s-SNOM method depends heavily on experimental conditions. We calculate $D_e\,(\omega, t)$ across a range of relevant frequencies and hBN thicknesses (Fig. S8b).

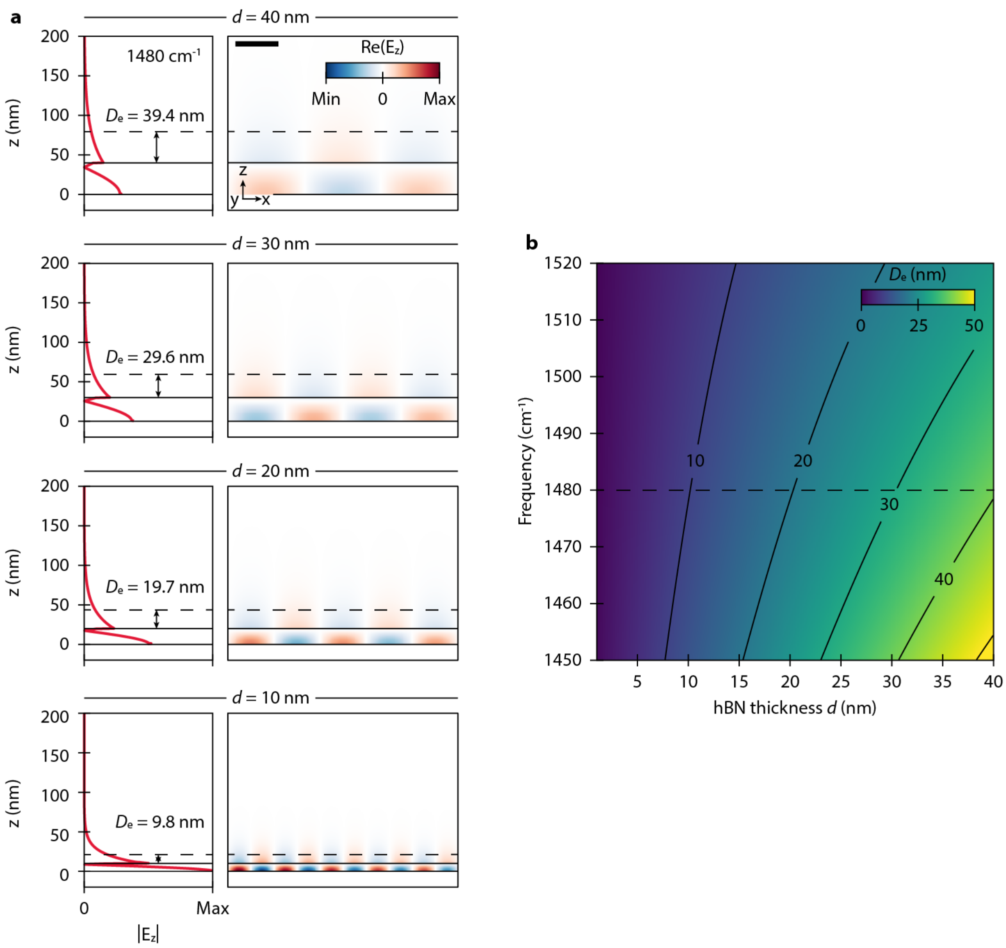

Figure S8. HIP mode field penetration depth. a, The $|E_z|$ profile of the HIP mode and the numerically calculated Re(E_z) field profile for thicknesses ranging from 40 to 10 nm. The profiles displays the field penetration depth $D_e = |E_{z=t}|\,\mathrm{e}^{-1}$ into free-space above the hBN. For all cases the excitation frequency is 1480 cm^{-1} (scale bar, 50 nm). **b**, Map of D_e for different hBN thicknesses versus frequency; the dashed line indicates the excitation frequency in (**a**).

S5. Nonlocal corrections to hBN

Throughout this work, we focus on the nonlocal effects in the metal layer under the assumption that the nonlocal effects in hBN are negligible. This assumption stems from the low group velocities of the longitudinal optical (LO) phonons in this material, which have been reported to be on the order of a few km/s – and therefore a few orders of magnitude lower than the Fermi velocity of electrons in Au.
To verify that this assumption is correct, in this section we quantify the nonlocal response of the hBN layer as a function of its thickness, while keeping the metal response as local. To do so, we start by considering the longitudinal permittivity of hBN to be written as [6]

$$\epsilon_{\mathrm{L},s}(\omega, k) = \epsilon_{\infty,s}\left(\frac{\omega_{\mathrm{LO},s}^2 - \omega^2 - \mathrm{i}\omega\Gamma_s - \beta_s^2 k^2}{\omega_{\mathrm{TO},s}^2 - \omega^2 - \mathrm{i}\omega\Gamma_s - \beta_s^2 k^2}\right), \tag{S9}$$

(see section S7.) where β_s is taken as the group velocity of the LO phonon in hBN along direction $s = \|, \perp$ with respect to the hBN layers. For simplicity, we neglect any dependence on β on momentum q and the thickness of the hBN layer, and take reference values $\beta_{\|} = 3$ km/s and $\beta_{\perp} = 1$ km/s.
From here, the adopted theoretical formalism follows closely the one described in section S1: we consider additional longitudinal solutions in the hBN layer which are characterized by a longitudinal wavevector k_{L}. However, since hBN permittivity is described by a Lorentzian function and is anisotropic, the shape of k_{L} differs from the one reported above for a metal, and should instead be taken from the solution of the equation

$$q^2\epsilon_{\mathrm{L},\|}(\omega, q) + k_{\mathrm{L}}^2\epsilon_{\mathrm{L},\perp}(\omega, k_{\mathrm{L}}) = 0, \tag{S10}$$

which has an analytical solution. Proceeding otherwise as described in section S1, we are able to obtain the results shown in Fig. S9.

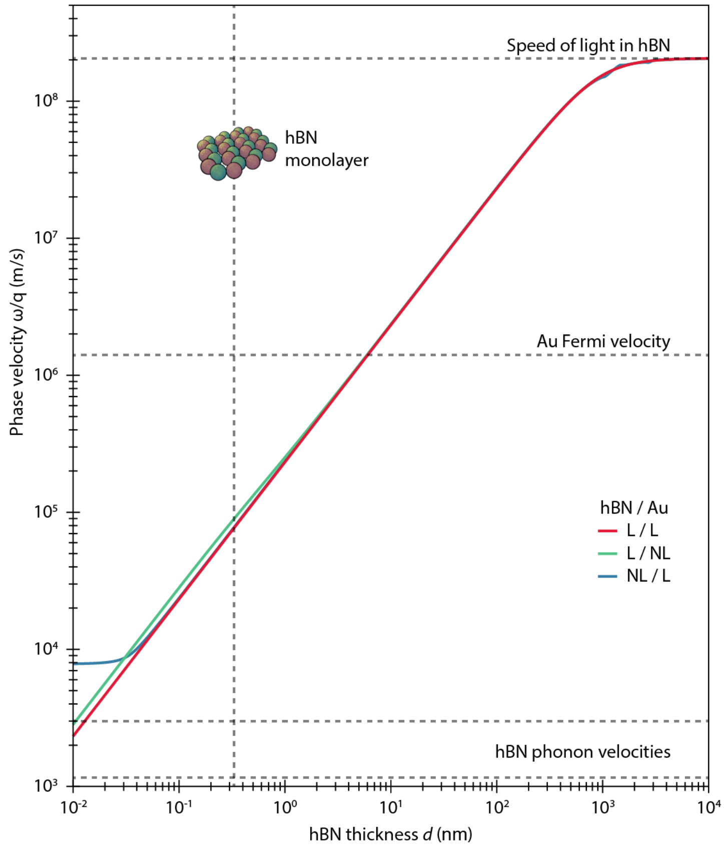

Figure S9. Nonlocality in hBN and its effect on HIP phase velocity. Effect of hBN thickness on HIP phase velocity at a frequency of 1500 cm^{-1}. Metal nonlocality (green line) causes a small perturbation to the phase velocity compared to the local case (red line), but hBN nonlocality has a significant impact (blue line) once the phase velocity is around 10^4 m/s.

We observe in Fig. S9 that, for all realistic hBN thickness values ($d \gtrsim 0.3$ nm), the curves with local and nonlocal hBN coincide perfectly. To observe a sizeable difference between the two, one needs to artificially reduce the thickness of this layer down to $d < 0.1$ nm, because only for such unrealistic thicknesses the phase velocity of the HIPs is comparable with the group velocity of the optical phonons in hBN. Nevertheless, the nonlocal effects in hBN quickly become stronger than those in Au, which is consistent with our hypothesis that the reduced role of Au nonlocality arises from the fact that most energy of the HIP is concentrated in the hBN layer (especially as d is reduced), which results on a stronger role of hBN nonlocality (akin to graphene nonlocality in the GSPs in Fig. 1 of the main text) once d is sufficiently reduced.
These results confirm that nonlocal effects in hBN can be safely neglected in our analysis, and further highlight that HIPs in hBN/Au heterostructures are excellent systems for achieving highly-confined modes that are weakly influenced by nonlocal effects.

S6. Near-field data analysis

Here we describe our approach for characterising near-field data, using as an example a sample with an AFM-measured hBN thickness of 14.4 ± 0.2 nm (Fig. S10a). The methodology we employ is similar to the one presented by Jang *et al.* [7], but is generalised for improved handling of multiple samples. Since multiple samples, with significantly varying hBN thickness, are used, the scanned area differs between samples but generally contains 200×200 pixels.

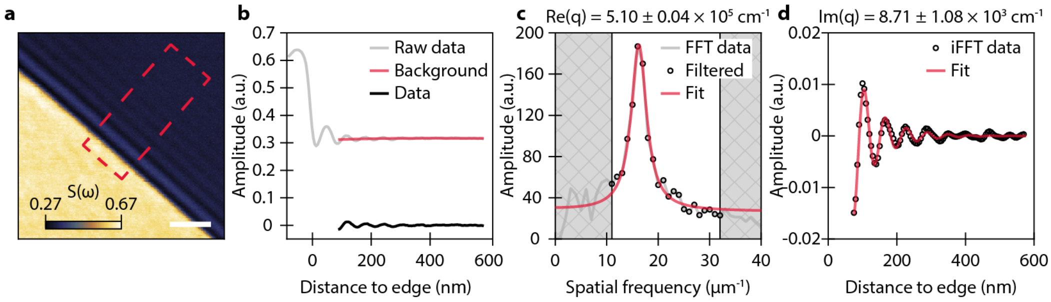

Figure S10. Procedure for analysing near-field fringes. a, Spatial plot of the s-SNOM measurement of a sample at a frequency of 1480 cm^{-1}. The red-bordered rectangle designate the line scan area (scale bar, 200 nm). **b,** Original profile (grey), background (red), and result of removing the background (black). The edge position is assumed to be the first intensity dip; therefore, we truncate the signal at the second dip. **c,** Fourier spectrum (grey line), to which a rectangular frequency filter is applied (black circles) and the fit (red line). **d,** Inverse Fourier transform of the black circles in **c** yields only the tip-launched polariton contribution (black circles) to which a damped harmonic oscillator is fitted (red line).

1. *Extract fringes.* We perform line scans perpendicular to the hBN edge to extract data from the third harmonic demodulated s-SNOM plots (Fig. S10a,b). Each line scan averages over multiple parallel lines, typically corresponding 50 pixels in thickness. We truncate the signal at the first fringe, so that only the second fringe and beyond are included in the analysis. This exclusion helps eliminate parasitic near-field signals caused by strong scattering at the hBN edge.

2. *Background removal.* The near-field data contains background signals resulting from the self-interference of incident light and the excitation of surface-plasmon-polaritons in the hBN/Au heterostructure [7]. To remove this background, we fit a third-order polynomial to the fringe data and subtract it, setting the median to zero (Fig. S10b).

3. *Fast Fourier transform and fit.* We apply a fast Fourier transform (FFT) to each line scan, transforming the data into the spatial-frequency domain (Fig. S10c). The tip-launched mode appears as a clear peak in the spectrum, providing the polariton wavevector Re(q). To ensure an accurate read, however, we first apply a rectangular frequency filter with a width of $1.5\times$FWHM on the left side and $4 \times$ FWHM on the right side. This filtering effectively removes the edge-launched component while retaining the tail of the tip-launched mode for fitting.

   Next, we fit the filtered spectrum. Since the $|\mathbf{E}|$ profile of the launched polaritons follows a damped harmonic oscillator [ref], we fit the Fourier-transformed data with *:

$$F(s) = A\left(\frac{\gamma + \mathrm{i}s}{(\gamma + \mathrm{i}s)^2 + k^2}\right) + C, \tag{S11}$$

   where γ is the polariton damping rate, k is the spatial frequency, and C is a constant. Fitting Eq. (S11) to the Fourier spectrum yields Re(q) = $2\pi k$.

4. *Inverse fast Fourier transform and fit.* Finally, we extract Im(q) by correcting for the geometric decay factor associated with the radial waves of the tip-launched polariton. This is achieved by performing an inverse FFT on the filtered signal, isolating the contribution from the tip-launched mode. We then fit the near-field pattern with a damped harmonic oscillator model that accounts for the geometrical decay (Fig. S10d):

$$f(x) = A\frac{\mathrm{e}^{-4\pi\gamma x}\cos(4\pi x k)}{\sqrt{2(x + \lambda/2)}}, \tag{S12}$$

   where λ is the polariton wavelength (i.e. $\lambda = 1/k$) and is introduced in the geometric decay correction term $\sqrt{2(x + \lambda/2)}$ to make it dimensionless and remove the divergence that would otherwise happen when $x = 0$.

   The result of fitting equation (S12) provides Im(q) = $2\pi\gamma$, while also acting as a cross-check of Re(q) obtained using Eq. (S11).

S7. Dielectric function of hBN

The dielectric function of a polar material like hBN is generally well-described by a Lorentzian oscillator model of the 'TO-LO' form; therefore, the permittivity of both the in- and out-of-plane optical phonon modes follows:

$$\epsilon_{\mathrm{hBN},s}(\omega) = \epsilon_{\infty,s}\left(\frac{\omega_{\mathrm{LO},s}^2 - \omega^2 - \mathrm{i}\omega\Gamma_s}{\omega_{\mathrm{TO},s}^2 - \omega^2 - \mathrm{i}\omega\Gamma_s}\right), \tag{S13}$$

where ω is the frequency, ϵ_∞ is the high-frequency permittivity, ω_{TO} and ω_{LO} are the transverse optical (TO) and longitudinal optical (LO) phonon frequencies, and Γ is the phonon damping. These parameters depend on the isotopic composition of hBN [8], necessitating their precise determination.

* The $|\mathbf{E}|$ near-field fringes follow a damped harmonic oscillator:

$$\begin{aligned} f(x) &= A\mathrm{e}^{-2\pi\gamma x}\cos(2\pi k x) \\ &= A\mathrm{e}^{-2\pi\gamma x}\frac{\mathrm{e}^{\mathrm{i}2\pi k x} + \mathrm{e}^{-\mathrm{i}2\pi k x}}{2}. \end{aligned} \tag{*1}$$

Fourier transforming:

$$\begin{aligned} F[f(x)] &= \frac{A}{2}\left[\int_0^\infty \mathrm{e}^{-2\pi\gamma x}\mathrm{e}^{-\mathrm{i}2\pi(s-k)x}\,dx + \int_0^\infty \mathrm{e}^{-2\pi\gamma x}\mathrm{e}^{-\mathrm{i}2\pi(s+k)x}\,dx\right] \\ &= \frac{A}{2}\left[\frac{1}{2\pi\gamma + \mathrm{i}2\pi(s-k)}\,\frac{1}{2\pi\gamma + \mathrm{i}2\pi(s+k)}\right], \end{aligned} \tag{*2}$$

which reduces to Eq. (S11), where we add a constant C for fitting purposes.

Employing Raman spectroscopy (LabRAM HR Evolution from HORIBA using a 514 nm laser source), we measure the E_{2g} Raman-active mode, corresponding to the in-plane ω_{TO}, which we find to be 1364.3 cm^{-1} (Fig. S11). This TO phonon frequency corresponds to an isotopic composition of around $B^{10} : B^{11} = 20 : 80$, allowing us to determine the out-of-plane components of the dielectric function from literature data [8].

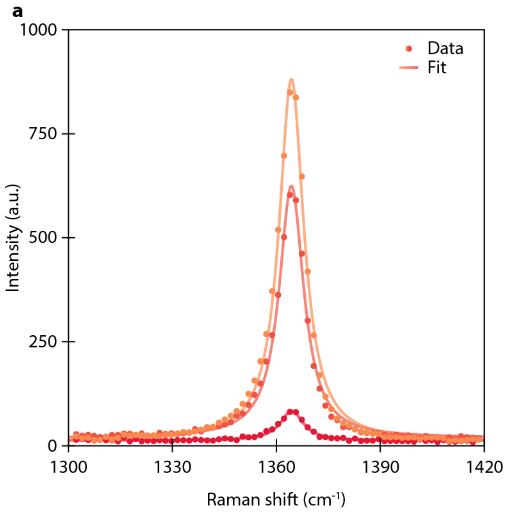

Figure S11. Raman spectra of hBN. 514 nm Raman spectra of the E_{2g} mode from three different hBN flakes and their corresponding four-parameter Lorentzian fit, all with a phonon peak at 1364.3 cm^{-1}.

To extract the remaining parameters – namely, the in-plane ϵ_∞, ω_{LO}, and Γ – we conduct s-SNOM measurements of multiple hBN flakes of varying thickness on silicon (Si) substrates (Fig. S12a). From these measurements, using our characterisation methodology (Section S6.), we are able to precisely extract the measured q and fit the dispersion of both the theoretical $\mathrm{Re}(q)$ and $\mathrm{Im}(q)$ (Fig. S12b,c). The fit of $\mathrm{Re}(q)$ align well with the measurements, with only one outlier (the 32 nm thick hBN sample at a frequency of 1500 cm^{-1}). Additionally, while the error bars for $\mathrm{Im}(q)$ are relatively larger, the fit remains consistent with our measurements and reveals low loss in the employed naturally abundant hBN.

The parameters of Eq. (S13) are summarised in Table S2. The optical constants for Si were obtained from the literature [9], with a 1.5 nm native silicon oxide (SiO_2) layer included [5], also adopting its constants from the literature [10].

Table S2. In-plane and out-of-plane parameters for the Lorentzian dielectric function of hBN, Eq. (S13).

	ϵ_∞	ω_{LO} (cm^{-1})	ω_{TO} (cm^{-1})	Γ (cm^{-1})
In-plane	5.22	1619.8	1364.3	3.5
Out-of-plane	2.25	820.2	761	2

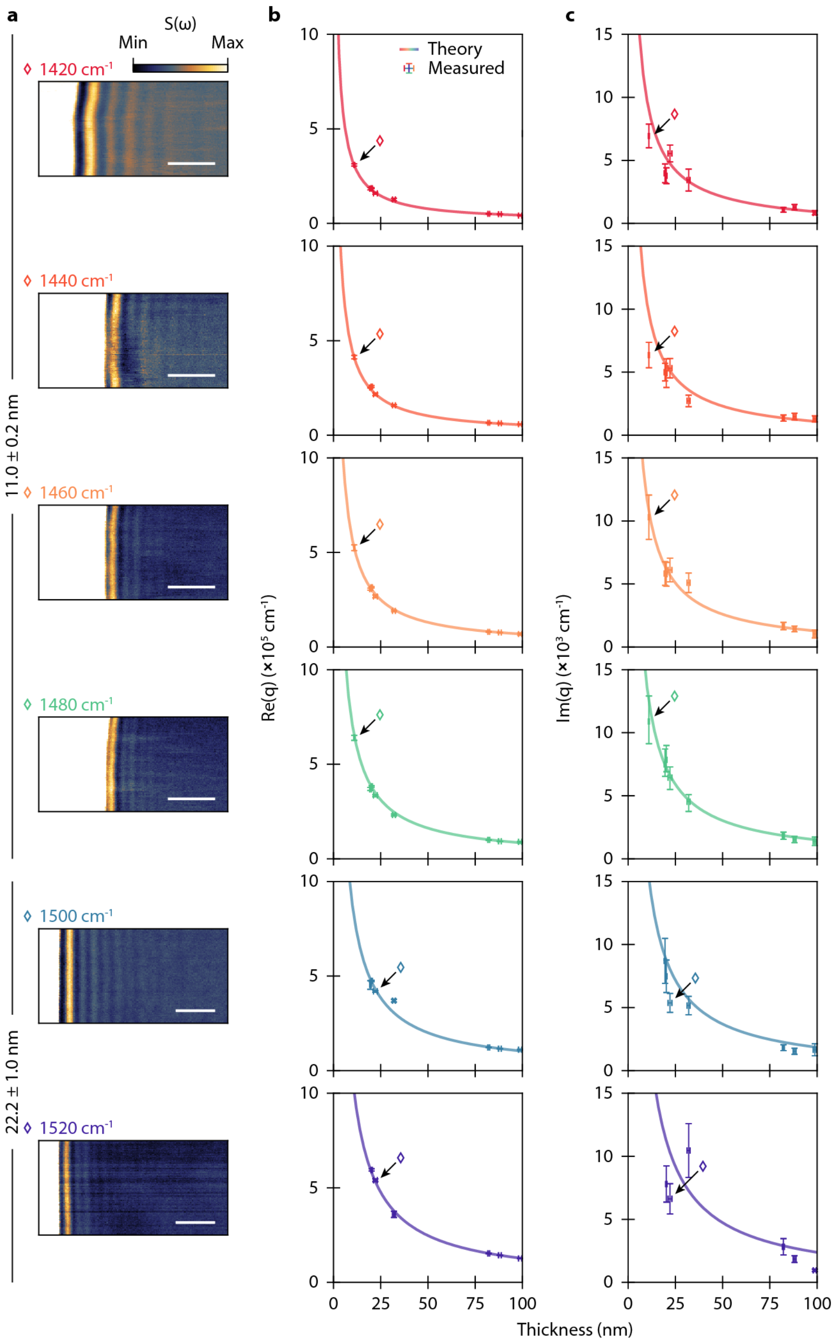

Figure S12. Dielectric function fit of hBN. a, Spatial plots of selected s-SNOM measurements where the amplitude has been saturated over the SiO_2/Si region for illustrative purposes (scale bars, 250 nm). **b,c**, Measured (markers) and fit (lines) of Re(q) (**b**) and Im(q) (**c**) as a function of hBN thickness in an hBN/SiO_2/Si heterostructure for various frequencies (wavenumbers).

S8. Transmission electron micrograph

Figure S13 shows cross-sectional scanning transmission electron microscope (STEM) images of an hBN-Au heterostructure, prepared from a sample featuring an hBN flake with a thickness of about 13.1 nm and a 1.9 nm interfacial layer. The analysis combines annular dark-field STEM (ADF-STEM) and high-resolution TEM (HR-TEM) to compare them. The sample is prepared as described in the Methods section and imaged with a JEOL-ARM300F operating at an accelerating voltage of 160 keV. ADF-STEM is particularly effective for imaging Au, as its high atomic number enhances scattering and provides excellent element contrast (Fig. S13a). However, this technique is less suitable for detecting defects or contamination within or next to low atomic number dielectrics, such as hBN (Fig. S13b). Accordingly, we emphasise the importance of combining ADF-STEM and HR-TEM to achieve a comprehensive understanding of most nanophotonic systems.

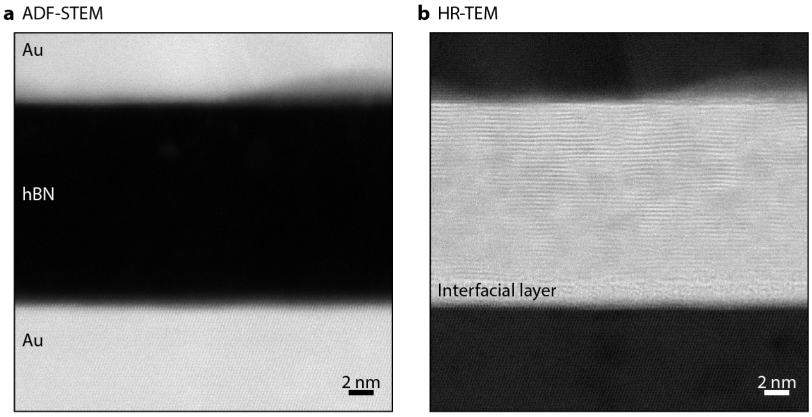

Figure S13. Cross-sectional transmission electron micrograph of the hBN-Au heterostructure. From bottom to top the images show monocrystalline Au, interfacial layer, hBN, and thermally evaporated Au. The upper Au layer is used to encapsulate the sample, protecting it from contamination and ion beam damaging during FIB. **a**, Annular dark-field (ADF-STEM) imaging of the sample. **b**, high-resolution (HR-TEM) imaging of the sample.

S9. Surface roughness

The surface roughness of the target monocrystalline Au flakes was measured, immediately before transfer of hBN, using the atomic force microscope (AFM) built into the s-SNOM employed for this study. Figure S14a shows AFM images of a Au flake directly after being cleaned with oxygen plasma (same as inset of Fig. 3b from the main paper), displaying an incredibly clean surface while also revealing terraces on the Au surface (these terraces likely stems from the synthesis process of the flakes), corresponding to the atomic spacing of Au – the step height of the terrace is ≈ 0.22 nm (Fig. S14b). By neglecting the terraces the root mean square (RMS) roughness was 44 pm. However, leaving the Au flake in ambient conditions for four days resulted in the gathering of a measurable surface layer on the Au (Fig. S14c) – even though the measured area is the same as in Fig. S14a, the terraces completely vanished, the surface got notably ”grainy”, and the RMS surface roughness increased to 95 pm. While such a surface roughness still appears to be state-of-the-art it is in fact a significant deterioration and hints at a formation of surface layers on crystalline Au.

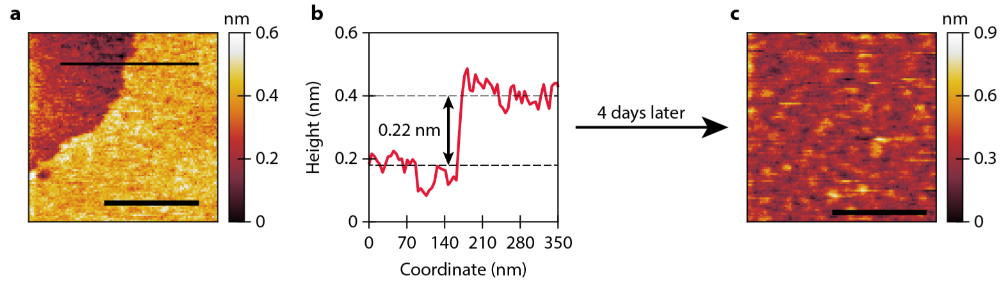

Figure S14. Surface roughness of a monocrystalline Au flake. a. AFM measurement revealing atomically flat terraces on the Au surface and a RMS surface roughness of 44 pm (terraces excluded). **b**. Line profile, indicated with a black line in (**a**), highlighting the terrace height being comparable to the atomic spacing of Au. **c**. AFM measurement of the same flake and area as in (**a**) but four days later. The RMS surface roughness was 95 pm (all scale bars, 250 nm).

S10. Interfacial layer refractive index

Based on literature we assume, in the main paper, that the interfacial layer has a refractive index of 1.2. To evaluate the sensitivity of the dispersion to the layer, we perform a numerical parametric sweep. Figure S15 shows the HIP dispersion relation for a 10 nm thick hBN layer, including a 2 nm interfacial layer with its refractive index swept from 1 to that of Au. The numerical calculations reveals that the dispersion is most sensitive when the index is close to 1.

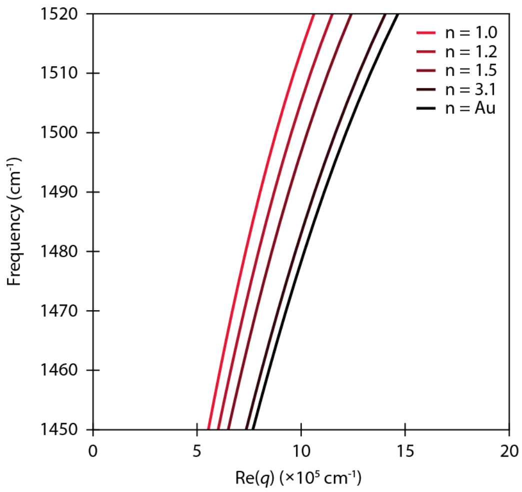

Figure S15. Refractive index sweep of 2 nm interfacial layer in the HIP configuration for a 10 nm thick hBN flake.

S11. Nonlocality in lower Reststrahlen band

It is well established that phonon-polaritons in the lower Reststrahlen band tend to be less screened by metallic substrates compared to their in-plane upper Reststrahlen band counterparts, due to the distinct electromagnetic boundary conditions and field distributions involved. For the sake of generality, we here calculate the nonlocal perturbation strength in the lower Reststrahlen band (frequency of 790 cm^{-1} in the middle of the band) and compare it to that of the upper band (Fig. S16), observing similarly minuscule nonlocal corrections. However, we also observe an interesting phenomenon: for the lower Reststrahlen band the nonlocal effects result in an increase in wavevector, in stark contrast to the decrease we observe for the upper band. As mentioned in the main paper, this apparent difference in behaviour is explained by the negative phase velocity of HIPs in the lower Reststrahlen band (with respect to the propagation direction), so in both cases the theoretical nonlocal effect corresponds to an introduced blueshift.

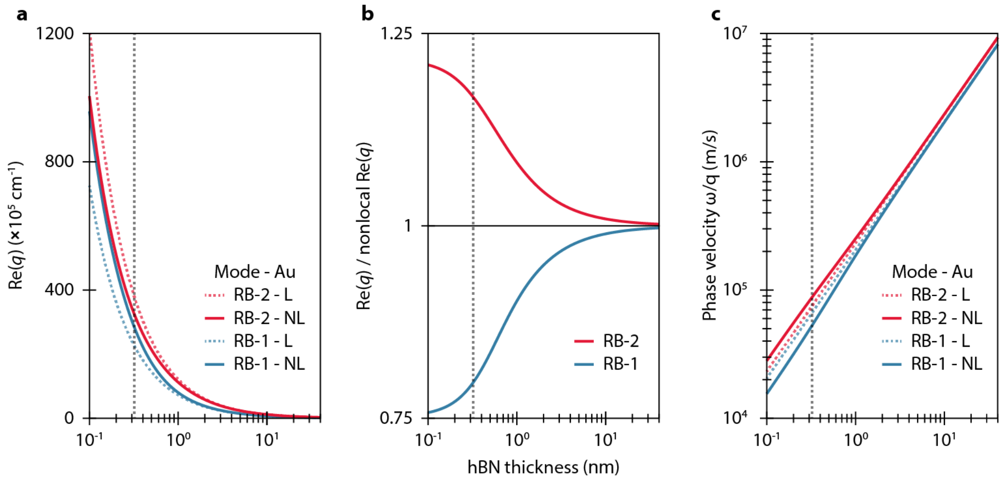

Figure S16. Nonlocal perturbation comparison between upper (RB-2) and lower (RB-1) Reststrahlen band. **a**, Theoretical predictions of Re(q) as a function of hBN thickness for a variety of cases at the frequencies of 1500 cm^{-1} and 790 cm^{-1}: RB-2 - L (local metal), RB-2 - NL (nonlocal metal), RB-1 - L, RB-1 - NL. **b**, Ratio of Re(q) for the local to nonlocal cases for the HIP modes. **c**, Phase velocity predictions corresponding to the cases shown in (**a**).

References

* asger@mailaps.org; jang.minseok@kaist.ac.kr;
J. T. H. and E. J. C. D. contributed equally to this work.

[1] E. J. C. Dias, D. A. Iranzo, P. A. D. Gonçalves, Y. Hajati, Y. V. Bludov, A.-P. Jauho, N. A. Mortensen, F. H. L. Koppens, and N. M. R. Peres, Physical Review B **97**, 245405 (2018).
[2] A. Moreau, C. Ciracì, and D. R. Smith, Physical Review B **87**, 045401 (2013).
[3] N. D. Mermin, Physical Review B **1**, 2362 (1970).
[4] D. A. Iranzo, S. Nanot, E. J. C. Dias, I. Epstein, C. Peng, D. K. Efetov, M. B. Lundeberg, R. Parret, J. Osmond, J.-Y. Hong, J. Kong, D. R. Englund, N. M. R. Peres, and F. H. L. Koppens, Science **360**, 291 (2018).
[5] Y. Yang, D. Zhu, W. Yan, A. Agarwal, M. Zheng, J. D. Joannopoulos, P. Lalanne, T. Christensen, K. K. Berggren, and M. Soljačić, Nature **576**, 248 (2019).
[6] C. R. Gubbin and S. De Liberato, Physical Review X **10**, 021027 (2020).
[7] M. Jang, S. G. Menabde, F. Kiani, J. T. Heiden, V. A. Zenin, N. A. Mortensen, G. Tagliabue, and M. S. Jang, Physical Review Applied **22**, 014076 (2024).
[8] A. J. Giles, S. Dai, I. Vurgaftman, T. Hoffman, S. Liu, L. Lindsay, C. T. Ellis, N. Assefa, I. Chatzakis, T. L.

Reinecke, J. G. Tischler, M. M. Fogler, J. H. Edgar, D. N. Basov, and J. D. Caldwell, Nature Materials **17**, 134 (2018).

[9] H. H. Li, Journal of Physical and Chemical Reference Data **9**, 561 (1980).

[10] J. Kischkat, S. Peters, B. Gruska, M. Semtsiv, M. Chashnikova, M. Klinkmüller, O. Fedosenko, S. Machulik, A. Aleksandrova, G. Monastyrskyi, Y. Flores, and W. T. Masselink, Applied Optics **51**, 6789 (2012).